Adaptive Eigenspace Regularization For Inverse Scattering Problems

M. J. Grote and U. Nahum

Adaptive Eigenspace Regularization
For Inverse Scattering Problems

Marcus J. Grote and Uri Nahum
Department of Mathematics and Computer Science,
University of Basel, Basel, Switzerland

August 31, 2017

Abstract

A nonlinear optimization method is proposed for inverse scattering problems in the frequency domain, when the unknown medium is characterized by one or several spatially varying parameters. The time-harmonic inverse medium problem is formulated as a PDE-constrained optimization problem and solved by an inexact truncated Newton-type method combined with frequency stepping. Instead of a grid-based discrete representation, each parameter is projected to a separate finite-dimensional subspace, which is iteratively adapted during the optimization. Each subspace is spanned by the first few eigenfunctions of a linearized regularization penalty functional chosen a priori. The (small and slowly increasing) finite number of eigenfunctions effectively introduces regularization into the inversion and thus avoids the need for standard Tikhonov-type regularization. Numerical results illustrate the accuracy and efficiency of the resulting adaptive eigenspace regularization for single and multi-parameter problems, including the well-known Marmousi problem from geophysics.

Keywords: Inverse medium problem, Helmholtz equation, full waveform inversion, PDE constrained optimization, multi-parameter estimation.

1   Introduction

Inverse scattering problems occur in a wide range of applications such as radar and sonar technology, non-destructive testing, geophysical exploration, and medical imaging. Given boundary data of scattered waves from an unknown inclusion, the scatterer, one seeks to determine its location, shape or physical properties. In general, the scatterer is a penetrable, bounded inhomogeneity inside the medium, which is characterized by one or several spatially varying physical parameters. The *inverse scattering (or inverse medium) problem* then consists in estimating these parameters from boundary measurements of the scattered wave field.

When qualitative information, such as the location or shape of the scatterer, is sought, various effective methods permit to quickly determine the support of the scatterer [4]. However, when quantitative information about the scatterer's physical properties, such as the local sound speed, is also needed, the inverse problems is typically reformulated as a PDE constrained optimization problem [34, 19, 31, 30, 20, 37, 24, 17], where the unknown

physical parameters are determined iteratively by minimizing an objective functional that measures the misfit between the simulated and the truly observed boundary data. While much research has focused on reconstructing a single spatially varying parameter, there is an increased interest in the solution of multi-parameter inverse problems, where at least two spatially varying parameters determine the physical properties of the medium. In oil and gas exploration, for instance, it is crucial to determine at least two parameters, such as density and bulk modulus [28, 32], to identify the elastic medium.

The inverse scattering problem is severely ill-conditioned, even more so in the multi-parameter case. Moreover, different parameters can influence each other thereby inducing spurious artifacts or "cross-talk" [29, 28]. To tackle the ill-posedness and ensure a stable (approximate) solution, the inverse problem is typically regularized by adding a *Tikhonov penalty term* to the misfit functional [35]. The choice for any particular norm used penalize the control variables through Tikhonov regularization [38, 33, 11] implicitly encodes a priori information about the scatterer's regularity. Moreover, Tikhonov regularization is rather sensitive to the size of the regularization parameter which controls the trade-off between the data misfit and the added penalty term: too small, the regularization will have too little effect; too large, the optimization will ignore the observations and simply minimize the penalty term. When the penalty functional itself involves additional parameters, such as in penalized total variation (TV) regularization [39, 12], determining appropriate parameter values for the reconstruction of a wide range of geophysical profiles, for instance, can be difficult [1].

Although Tikhonov regularization generally improves the stability of the inversion, it also retains all the control variables. Hence, the spatial discretization of the control parameter on a standard finite difference or finite element mesh typically leads to a prohibitively large number of (unknown) nodal values, in fact increasingly so as the mesh is further refined. Alternatively, *regularization by parametrization* [5] reduces significantly the number of control variables but also greatly improves on the stability by representing the unknown parameters themselves by a small number of basis functions. Without precise a priori knowledge about the scatterer, however, finding such a low-dimensional yet accurate representation for the unknown parameters is generally difficult.

For time-dependent scattering problems, an *adaptive eigenspace (AE) representation* proposed in [9, 8] achieved a significant reduction in the number of control variables by projecting the parameters to a finite-dimensional subspace spanned by the first eigenfunctions of a particular differential operator, iteratively adapted during the nonlinear optimization. By combining the AE representation with truncated inexact Newton-like methods [13, 10, 26, 24] and frequency stepping [6, 31], we proposed the Adaptive Eigenspace Inversion (AEI) method for single parameter inverse medium problems in the frequency domain, when the scattered wave field is governed by the Helmholtz equation [18]. Recently, de Buhan and Darbas developed an AEI method for electromagnetic inverse medium problems at fixed frequency [7].

Here, we extend our AEI approach to multi-parameter inverse problems in the frequency domain by building a separate basis of eigenfunctions for each parameter. More specifically, in Section 2, we consider a two-parameter inverse scattering model problem

and present in detail the AEI Algorithm in this multi-parameter setting. Next, in Section 3, we exhibit the fundamental connection between the AE representation and standard Tikhonov regularization, which enables us to devise other AE bases, each corresponding to a particular choice of Tikhonov penalty functional. Depending on the a priori available information about the smoothness properties or the (anisotropic) spatial dependency of the control parameters, we thus devise various AE bases for single and two-parameter inverse scattering problems in the frequency domain. Finally, in Section 4, we present a series of numerical experiments that illustrate the accuracy and efficiency of AE regularization for the inversion of single and multi-parameter inverse scattering problems.

2   Adaptive Eigenspace Inversion (AEI)

In this section, we consider a two-parameter acoustic inverse scattering problem where the scattered wave field is governed by the Helmholtz equation. We first formulate the inverse problem for the two (unknown) spatially varying parameters $u(x)$ and $v(x)$ as a PDE-constrained optimization problem. To regularize the ill-posed problem, u and v are projected each to a separate subspace spanned by a finite number of orthogonal eigenfunctions of a particular elliptic problem, the distinguishing feature of the AEI approach. We then provide a detailed description of the entire AEI algorithm.

2.1   Inverse medium problem

We consider a time-harmonic scattering problem from a penetrable inhomohogeneity inside an unbounded medium characterized by its compressibility, $v(x) > 0$, and its inverse density, $u(x) > 0$. Hence the local sound speed, $c(x) > 0$, is given by

$$c(x) = \sqrt{\frac{u(x)}{v(x)}}\,. \tag{1}$$

The scatterer is located inside a bounded convex domain $\Omega \subset \mathbb{R}^d$, $d = 1, 2, 3$. Outside Ω, both the compressibility, $v_\infty(x)$, and its inverse density, $u_\infty(x)$ are known and may vary. Inside Ω, the scattered field $y(x)$ satisfies the Helmholtz equation together with a Sommerfeld-type radiation condition at the (artificial) boundary $\Gamma = \partial\Omega$:

$$\begin{cases} -\omega^2 v(x)y(x) - \nabla \cdot (u(x)\nabla y(x)) &= f(x)\,, & \text{in } \Omega, \\ \dfrac{\partial y(x)}{\partial n} - ik(x)y(x) &= 0\,, & \text{on } \Gamma. \end{cases} \tag{2}$$

Here $\omega > 0$ denotes the time frequency, whereas $k(x) = \omega/c(x) > 0$ corresponds to the wave number.

Next, we perform N_s illuminations of the medium inside Ω with source terms $f = f_\ell$, $\ell = 1, ..., N_s$, and denote by y_ℓ the corresponding (unique) solutions of (2). Given the measurements y_ℓ^{obs} on Γ, or part of it, we seek to recover the (unknown) inverse density

$u(x)$ and compressibility $v(x)$ inside Ω, such that every solution y_ℓ of (2) with $f = f_\ell$ coincides at Γ with the measurements y_ℓ^{obs}, $\ell = 1, ..., N_s$. In doing so, we assume that both u and v are known and equal to $u_\infty(x)$ and $v_\infty(x)$, respectively, on the boundary Γ.

To solve the inverse medium problem, we now formulate it as a PDE-constrained optimization problem. Let

$$A[u,v]y = f$$

denote the forward Helmholtz operator in (2) for given u and v. Then we seek minimizers u and v of the standard L^2 data misfit functional,

$$\min_{u \in U, v \in V} \mathcal{F}(u,v) = \frac{1}{2} \sum_{\ell=1}^{N_s} \left\| PA[u,v]^{-1}f_\ell - \hat{y}_\ell \right\|^2, \tag{3}$$

where P denotes a projection operator onto the observational space.

To solve (3), we consider standard Newton or Quasi-Newton methods. Since the inverse problem (3) is severly ill-posed, Tikhonov regularization terms are typically first added for stability. In addition a third regularization operator may be added to prevent undesired artifacts between the parameters (cross-talk) [15]. Instead, we shall incorporate regularization by restricting u and v each to a separate finite-dimensional subspace, adaptively determined during the optimization.

2.2 Adaptive eigenspace expansion

Instead of a standard (FD, FE grid-based discretization) nodal basis, we shall use a separate basis of (global) eigenfunctions $\{\phi_m\}_{m \geq 1}$ and $\{\varphi_m\}_{m \geq 1}$ to represent $u(x)$ and $v(x)$, respectively:

$$u(x) = u_0(x) + \sum_{m=1}^{K_u} \beta_m \, \phi_m(x) \qquad v(x) = v_0(x) + \sum_{l=1}^{K_v} \gamma_l \, \varphi_l(x). \tag{4}$$

Following [18], we let the "background" $u_0(x) \in H^1(\Omega)$ solve the elliptic problem,

$$\begin{cases} -\nabla \cdot (\mu[u](x)\nabla u_0(x)) &= 0, &\forall\, x \in \Omega, \\ u_0(x) &= u_\infty(x), &\forall\, x \in \Gamma, \end{cases} \tag{5}$$

and similarly for $v_0(x)$ with $\mu[u]$ replaced by $\mu[v]$ and u_∞ replaced by v_∞. Here, $\mu[u](x)$ is defined by

$$\mu[u](x) = \frac{1}{\sqrt{|\nabla u(x)|^2 + \varepsilon^2}}, \qquad \forall\, x \in \Omega,\ \varepsilon > 0. \tag{6}$$

The parameter $\varepsilon > 0$, which ensures that the denominator of μ does not vanish, is typically set to a very small value such as $\varepsilon = 10^{-6}$. While the primary role of u_0 and v_0 is to accommodate the (known) inhomogeneous boundary values of u and v, we shall demonstrate in Section 3 that u_0 and v_0 also capture much of their behavior inside Ω.

4

For the functions ϕ_m, we choose the orthonormal basis of eigenfunctions $\phi_m \in H_0^1(\Omega)$ of the elliptic operator,

$$\begin{cases} -\nabla \cdot (\mu[u](x)\nabla\phi_m(x)) &= \lambda_m\phi_m(x), & \forall\, x \in \Omega, \\ \phi_m(x) &= 0, & \forall\, x \in \Gamma, \end{cases} \tag{7}$$

with corresponding eigenvalues $0 < \lambda_m \leq \lambda_{m+1}$, $m \geq 1$. Similarly, for the functions φ_m we choose the orthonormal basis of eigenfunctions $\varphi_m \in H_0^1(\Omega)$ of the elliptic operator,

$$\begin{cases} -\nabla \cdot (\mu[v](x)\nabla\varphi_m(x)) &= \tilde{\lambda}_m\varphi_m(x), & \forall\, x \in \Omega, \\ \varphi_m(x) &= 0, & \forall\, x \in \Gamma, \end{cases} \tag{8}$$

with corresponding eigenvalues $0 < \tilde{\lambda}_m \leq \tilde{\lambda}_{m+1}$, $m \geq 1$. Clearly, at higher λ_m or $\tilde{\lambda}_m$, the corresponding eigenfunctions ϕ_m or φ_m will be increasingly oscillatory.

In [18], we provided analytical and numerical evidence which underpins the remarkable accuracy of this basis for representing any given $u(x)$. In our AEI approach, the eigenfunctions $\{\phi_m\}_{m\geq 1}$ and $\{\varphi_m\}_{m\geq 1}$, together with the backgrounds u_0 and v_0, are repeatedly recomputed as the underlying control variables $u(x)$ and $v(x)$ vary during the optimization. Hence, we call $\{u_0\} \cup \{\phi_m\}_{m\geq 1}$ (and $\{v_0\} \cup \{\varphi_m\}_{m\geq 1}$) an adapted eigenspace (AE) basis.

Since $u(x)$ and $v(x)$ are precisely the quantities we seek, and thus unknown, we always use in (5)–(8) their current values from the previous optimization step. In the first step, when no information about u or v inside Ω is available yet, we simply set $\mu[u](x) \equiv \mu[v](x) \equiv 1$. Then, u_0 and v_0 reduce to harmonic prolongations of u_∞ and v_∞ from Γ into Ω, while the two bases $\{\phi_m\}_{m\geq 1}$ and $\{\varphi_m\}_{m\geq 1}$ both simply correspond to the eigenfunctions of the Laplacian operator in Ω. During subsequent steps, however, once u and v begin to differ, the two bases will also differ from each other.

2.3   AEI Algorithm

To keep both the memory requirements and the computational effort low, it is imperative to keep the numbers of eigenfunctions K_u and K_v in (4) minimal. Yet the truncation of the eigenfunction expansion is also crucial for numerical stability, as it builds regularization into the AEI approach.

At higher frequencies, waves detect and carry more detailed information about the scatterer, though the number of local minima of $L[u]$ may also increase. To minimize the chance of landing in a (false) local minimum, we also apply a standard frequency continuation procedure [6, 2]. First, we solve the inverse problem (3) at the lowest frequency ω_1. Then we progressively increase $\omega = \omega_2, \ldots, \omega_n$ while re-initializing the optimization at every ω_j from the solution u of the previous lower frequency ω_{j-1}. In doing so, we assume that the measurements are available through a range of frequencies, for instance via Fourier transform of a time-dependent signal.

AEI Algorithm.
Input: initial guess $u = 1$, $v = 1$, observations y_ℓ^{obs}. Output: u^*, v^*.

1. Choose $K_u \geq 1$, $K_v \geq 1$. Compute $\{\phi_m\}_{m=1}^{K_u}$, $\{\varphi_m\}_{m=1}^{K_v}$ from (7), (8) and u_0, v_0 from (5) with $\mu[u] \equiv \mu[v] \equiv 1$

2. Expand $u(x) = u_0(x) + \sum_{m=1}^{K_u} \beta_m \phi_m(x)$ and $v(x) = v_0(x) + \sum_{l=1}^{K_v} \gamma_l \varphi_l(x)$

3. For $\omega = \omega_1, \ldots, \omega_n$

   (a) Compute $\mathcal{F}[u,v]$ and $\nabla\mathcal{F}[u,v]$, set H to the (approx.) Hessian

   (b) While $\|\mathcal{F}[u,v]\| \geq \text{tol}$

      i. Solve $Hp = -\nabla\mathcal{F}[u,v]$ with truncated CG

      ii. Determine step size α and update $[u,v] \leftarrow [u,v] + \alpha p$

      iii. Update $\mathcal{F}[u,v]$, $\nabla\mathcal{F}[u,v]$ and H

   (c) Set $\mu[u]$ and $\mu[v]$ as in (6) using current u, v

   (d) Update K_u, K_v, compute $\{\phi_m\}_{m=1}^K$ and $\{\varphi_m\}_{m=1}^{K_v}$ from (7), (8) and u_0, v_0 from (5)

   (e) Expand $u(x) = u_0(x) + \sum_{m=1}^{K_u} \beta_m \phi_m(x)$, $\quad v(x) = v_0(x) + \sum_{l=1}^{K_v} \gamma_l \varphi_l(x)$

4. Set $u^* = u$

The AEI approach applies regardless of the underlying optimization method used. Here we consider truncated Newton-like methods [10, 26] and denote by H either the true Hessian or some approximation of it, depending on the (Newton or Gauss-Newton) method used. In all cases the linear system in Step 3(b) is solved by a truncated CG-iteration with the Eisenstat-Walker criterion [13]. In Step 3(b)ii, the step size α of the search direction p is determined through Armijo step-size control. In Steps 1 and 3(d) of the AEI Algorithm, we compute the first K_u or K_v eigenfunctions in (7) or (8) by using a standard restarted Lanczos iteration [22].

3   Adaptive eigenspace regularization

The AEI approach inherently builds regularization into the optimization by restricting the search space to the span of finitely many eigenfunctions of the elliptic eigenvalue problems (7), (8). In fact, the elliptic operator in (7) (or (8)) coincides with the gradient of the penalized total variation (TV) regularization term [33, 39],

$$R_{TV}[u] = \frac{1}{2} \int_\Omega \sqrt{|\nabla u|^2 + \varepsilon^2} \, dx, \tag{9}$$

since

$$\begin{aligned}
\nabla R_{TV}[u] &= -\nabla \cdot \left(\frac{1}{\sqrt{|\nabla u|^2 + \varepsilon^2}} \nabla u \right) \\
&= -\nabla \cdot (\mu[u](x)\nabla u),
\end{aligned}$$ (10)

with $\mu[u]$ as in (6). Equation (10) thus yields the fundamental connection between the AE and Tikhonov regularization.

Hence, the AEI approach offers an alternative to standard Tikhonov regularization [35, 16, 14], where a penalization term $\alpha\,\mathcal{R}[u,v]$ is added to the objective functional in (3). In Tikhonov regularization, the choice of the parameter α is critical: if α is too small, the penalty term will provide too little regularization whereas if α is too large, the objective functional will essentially ignore the data misfit. Striking the right balance between these two competing effects is difficult a priori and usually involves some trial-and-error for any particular problem [1].

Penalized TV-regularization is well-known in image processing because it achieves noise removal while preserving sharp interfaces. Since the AEI approach projects u to the basis of eigenfunctions determined by the gradient of the penalized TV-regularization functional, the AE basis inherits similar properties. Not surprisingly, that choice proved judicious for the solution of inverse Helmholtz problems in the presence of a discontinuous medium and noisy data [18]. Still, many other penalty functionals $\mathcal{R}[u]$ can be used with Tikhonov regularization [38], as each particular choice captures specific prior knowledge about the unknown parameter u. Each particular penalty functional will also lead to a different AE basis apt to efficiently represent the same class of functions as that determined by the corresponding Tikhonov regularization term. For illustration, we now compute the spatially varying coefficient $\mu[u](x)$ for the H^1, Gaussian and Lorentzian penalty functionals – see [25] for details.

First, we consider the H^1-penalty functional,

$$\mathcal{R}_{\nabla u}(u) = \frac{1}{2}\|\nabla u\|_{L^2(\Omega)},$$ (11)

which penalizes strong variations in u and hence is well adapted to smooth profiles. Its gradient is given by

$$\begin{aligned}
\nabla R_{\nabla u}[u] &= -\Delta u \\
&= -\nabla \cdot (\mu[u](x)\nabla u),
\end{aligned}$$

for $\mu[u] = 1$ identically. Hence the corresponding elliptic eigenvalue problem reduces here to

$$\begin{cases}
-\Delta\phi_m(x) &= \lambda_m\phi_m(x), & x \in \Omega, \\
\phi_m(x) &= 0, & x \in \Gamma.
\end{cases}$$ (12)

The AE basis corresponding to the H^1-penalty functional thus merely consists of the standard eigenfunctions of the Laplacian, whose Fourier expansion is well-known to rapidly converge for smooth profiles. Hence, it inherits its approximation properties from the H^1-penalty functional; in this special case, the eigenfunctions are actually independent of u.

The H^1-penalty functional can easily be generalized to more complex anisotropic media, as in seismic imaging, by replacing the gradient in (11) by another more appropriate differential operator [16] – see Section 4.2.

Second, we consider the (non-convex) Gaussian penalty term [12],

$$R_{Gauss}(u) = \frac{1}{2} \int_\Omega 1 - \exp\left(-\frac{|\nabla u|^2}{\sigma^2}\right) \, dx \,, \quad \sigma > 0 \,. \tag{13}$$

Its gradient is given by

$$\nabla_u \mathcal{R}_{Gauss}(u) = -\nabla \cdot \left(\frac{\nabla u}{\sigma^2 \, \exp\left(-|\nabla u|^2/\sigma^2\right)}\right) \,, \quad \sigma > 0 \,, \tag{14}$$

and thus leads to the elliptic eigenvalue problem (7) with

$$\mu[u](x) = \frac{1}{\sigma^2 \, \exp\left(|\nabla u|^2/\sigma^2\right)} \,, \quad \sigma > 0 \,. \tag{15}$$

Here μ truly depends on u, as it does for penalized TV-regularization (6), and therefore the AE eigenspace will be adapted in each step of the AEI Algorithm.

Third, we consider the (non-convex) Lorentzian penalty term,

$$R_{Lorentz}(u) = \frac{1}{2} \int_\Omega \frac{\gamma|\nabla u|^2}{1 + \gamma|\nabla u|^2} \, dx \,, \quad \gamma > 0 \,, \tag{16}$$

whose extra parameter γ permits strong variations in u. Its gradient is given by

$$\nabla_u \mathcal{R}_{Lorentz}(u) = -\nabla \cdot \left(\frac{\gamma \nabla u}{(1 + \gamma|\nabla u|^2)^2}\right) \,, \quad \gamma > 0 \,, \tag{17}$$

and thus leads to the elliptic eigenvalue problem (7) with

$$\mu[u](x) = \frac{\gamma}{(1 + \gamma|\nabla u|^2)^2} \,, \quad \gamma > 0 \,. \tag{18}$$

Remark: The standard Tikhonov L^2-*penalty* functional,

$$\mathcal{R}_{L^2}(u) = \frac{1}{2} \|u\|_{L^2}^2 \,, \tag{19}$$

leads to the trivial eigenvalue problem for the identity operator. Therefore, it neither defines a unique orthogonal set of eigenfunctions nor yields a useful basis for the AEI approach.
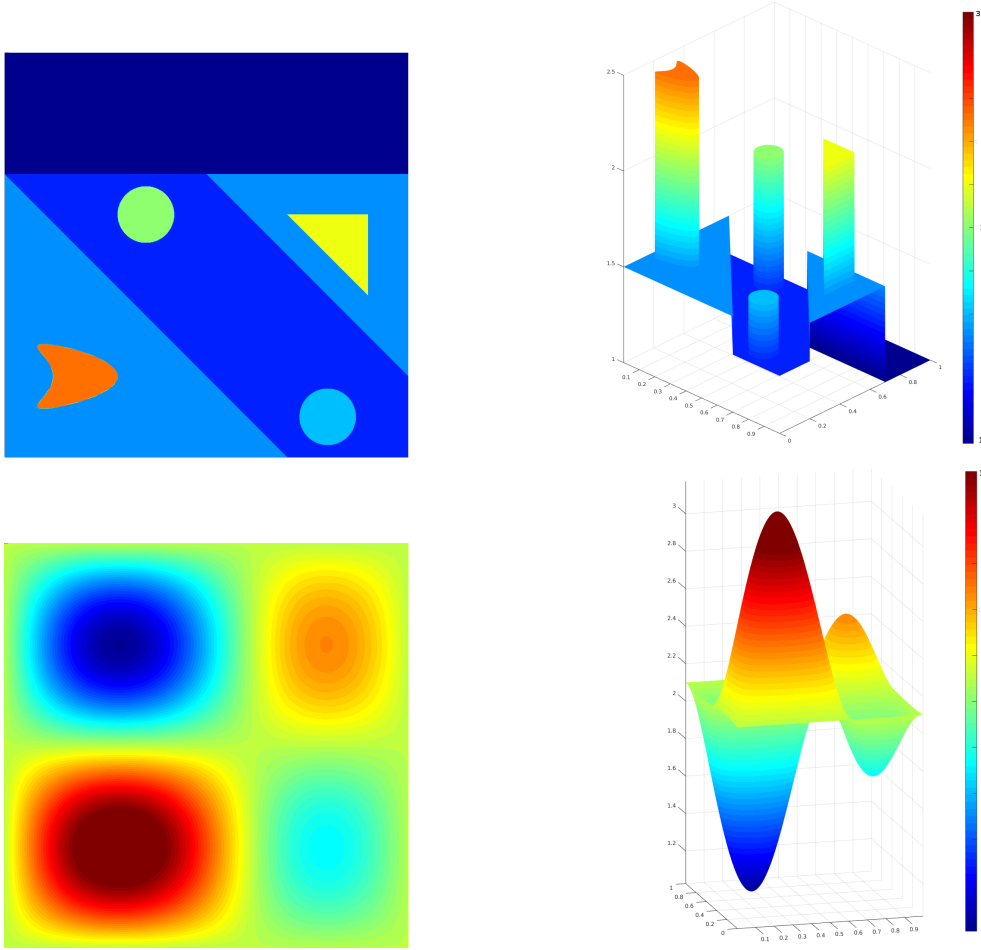
Figure 1: Two-dimensional medium u: piecewise constant (top), and smooth asymmetric profile (bottom). Top view (left) and three-dimensional view (right).

3.1 Two-dimensional numerical examples

To illustrate not only the remarkable approximation properties of the AE basis but also the effect of any particular choice of penalty functional, we now consider the two-dimensional profiles $u(x)$ shown in Fig. 1: The first, piecewise constant, mimics a layered background material with local inclusions, whereas the second corresponds to a smooth asymmetric profile. For each of the previously described penalty functionals, we now compute the background u_0 from (5) together with the first four eigenfunctions $\phi_1, \ldots, \phi_4$ from (7) using the corresponding coefficient $\mu[u]$. Then we use this five-dimensional AE basis to compute its best L^2-approximation and compare it with u to evaluate its accuracy in representing the given profile.

First, we consider the piecewise constant profile u shown at the top of Fig. 1 and compute the AE basis corresponding to TV-regularization: Hence, we compute the background u_0 from (5) together with the first four eigenfunctions $\phi_1, \ldots, \phi_4$ from (7), both
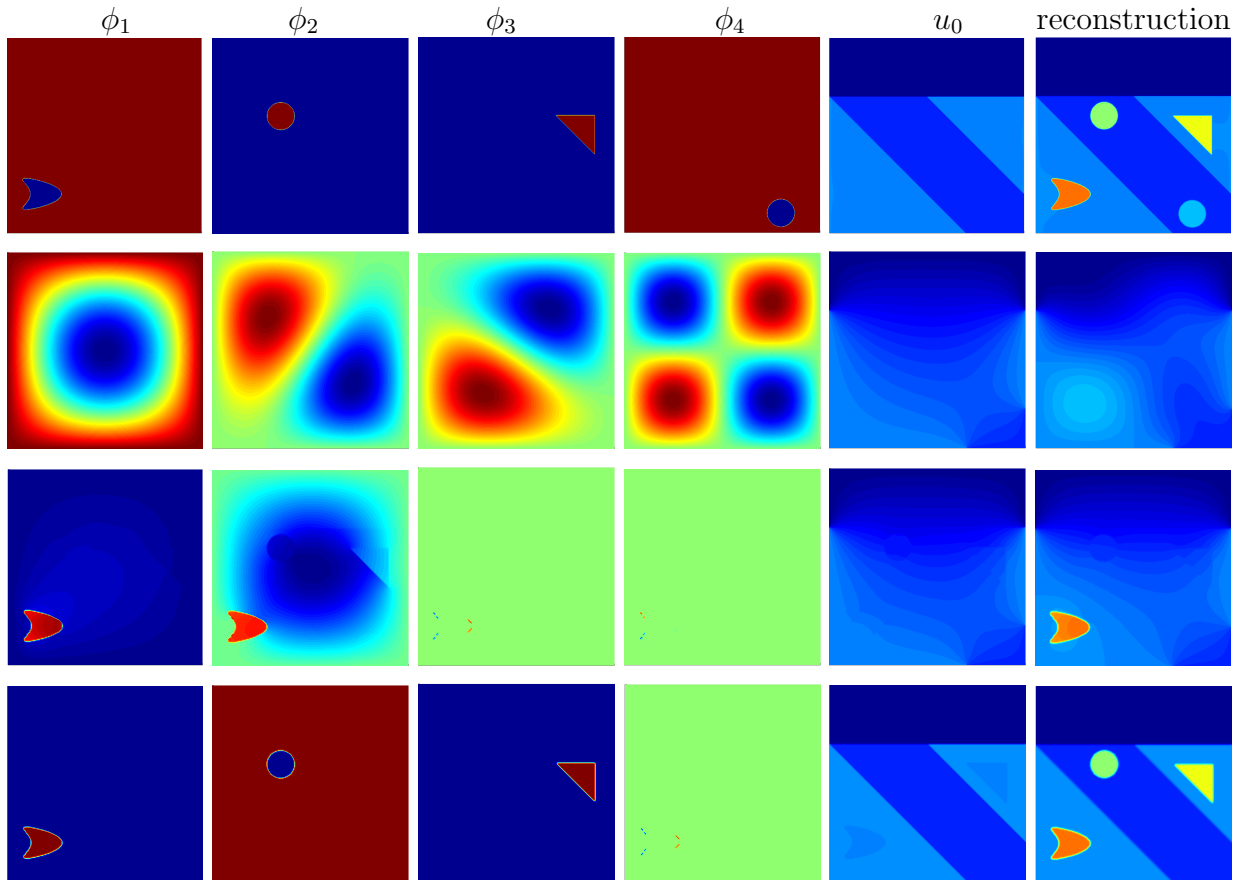
Figure 2: Piecewise constant two-dimensional profile. From top to bottom: TV-regularization, H^1-regularization, Gaussian regularization and Lorentzian regularization. From left to right: the first four AE eigenfunction ϕ_1, ϕ_2, ϕ_3, ϕ_4, the background u_0, the best L^2-approximation of u using ϕ_1, ..., ϕ_4 and u_0.

with $\varepsilon = 10^{-6}$ and μ as in (6). In Fig. 2, we observe how u_0 matches with remarkable accuracy the background medium but misses the different embedded obstacles. The first four eigenfunctions ϕ_1, ..., ϕ_4, however, ignore the background and capture precisely the remaining obstacles. Using u_0 and ϕ_1, ..., ϕ_4, we now expand u as in (7) with $K_u = 4$ and compute its best L^2-approximation. Shown in Fig. 2, it is hardly distinguishable from the true u in Fig. 1 with well-defined sharp contours and a relative L^2-error below 1.9%. These results demonstrate the accuracy even of but a few eigenfunctions of the TV-regularization based AE basis for a piecewise constant layered medium with isolated obstacles.

In contrast, if we repeat the same experiment for H^1-regularization using (11) with $\mu \equiv 1$, we observe in the second line of Fig. 2 how u_0 indeed matches the boundary values of u but otherwise fails to capture any additional features inside Ω. Moreover, the best approximation of u with respect to these five basis functions hardly correlates with the true medium and leads to a ninefold increase in the relative L^2 error up to 16.2%. The poor accuracy obtained with the eigenfunctions of the Laplacian is to be expected here,
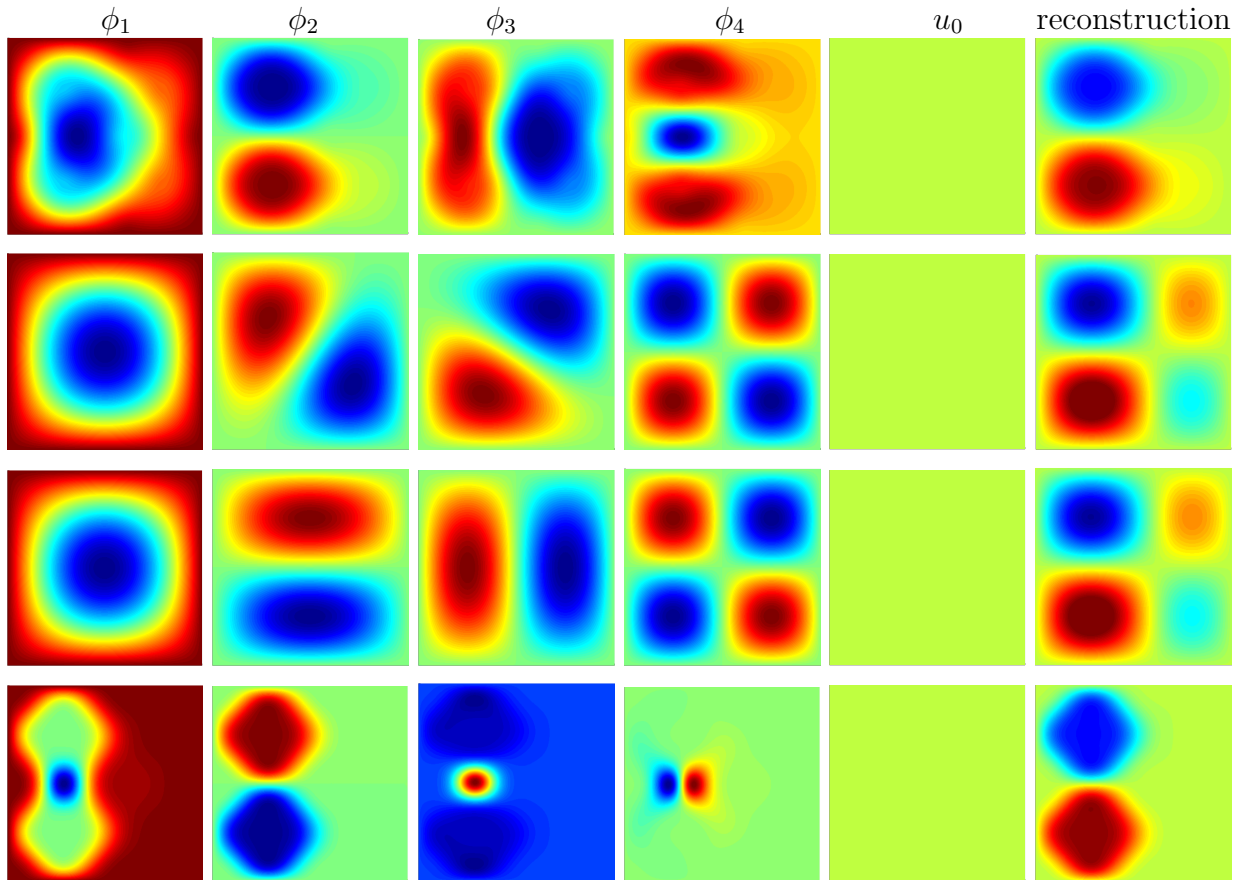
Figure 3: Smooth asymmetric two-dimensional profile. From top to bottom: TV-regularization, H^1-regularization, Gaussian regularization and Lorentzian regularization. From left to right: the first four AE eigenfunction ϕ_1, ϕ_2, ϕ_3, ϕ_4, the background u_0, the best L^2-approximation of u using $\phi_1, \ldots, \phi_4$ and u_0.

since they correspond to H^1-regularization which penalizes non-smooth profiles.

We now repeat the above experiment for Gaussian regularization (14) with $\sigma = 70$ and Lorentzian regularization (16) with $\gamma = 250$ using the AE basis with $\mu[u](x)$ given by (15) or (18), respectively. In both cases, the L^2 best approximation matches only part of the medium. The relative L^2-error is 13% for the Gaussian and 3.3% for the Lorentzian best AE approximation. Although the five-dimensional Lorentzian AE reconstruction captures only three (from a total of four) embedded obstacles, it also captures the fourth when further eigenfunctions are added.

Next, we consider the smooth asymmetric profile u shown at the bottom of Fig. 1 and repeat the above numerical experiments. In contrast to the previous piecewise constant case, the approximation using the H^1 or the Gaussian adaptive eigenspaces are now the most accurate with a relative L^2-error of 0.002% for the H^1 and of 0.036% for the Gaussian AE best approximation. As shown in Fig. 3, the AE bases for TV or Lorentzian regularization are now less accurate with relative L^2-errors of 8.1% or 6.5%, respectively.

In summary, these numerical results demonstrate how different penalty functions lead to different AE bases which distinct approximation properties. While the TV based AE representation is particularly efficient for piecewise constant media with isolated obstacles, H^1 based regularization is a judicious choice for smooth profiles. Hence, prior knowledge about the medium can be included into the optimization through any particular choice of the AE basis.

4   Numerical Results

We shall now illustrate the usefulness and versatility of the AEI method through a series of numerical experiments. First we consider a single parameter inverse problem with the inverse density $u(x)$ from Section 3 and fixed compressibility $v(x) \equiv 1$. Clearly the control $u(x)$ is now unknown. We compare the AE representation to a standard grid-based nodal representation of $u(x)$ to demonstrate the resulting significant reduction in degrees of freedom. Next, we consider the well-known Marmousi profile from geosciences which models a typical layered medium from the Earth's subsurface. By incorporating the a priori knowledge about the medium's anisotropy directly into the AE basis, we further improve upon its accuracy. Finally, we consider a two-parameter inverse medium problem to demonstrate the improvement in accuracy and, in particular, the significant reduction in spurious "cross-talk" between the control parameters $u(x)$ and $v(x)$ thanks to the AE representation.

Unless specified otherwise, we illuminate the medium from equispaced Gaussian sources located at a fixed distance from the top boundary, whereas the receivers are located on the four lateral boundaries of $\Omega = (0, 1) \times (0, 1)$. Inside Ω we use second-order staggered finite difference on an regular Cartesian mesh for the discretization of (2) and (5)–(7). To avoid any inverse crime, the reference solution is computed on a separate finer mesh, which does not contain the computational mesh.

For the inversion, we always use the AEI Algorithm as described in Section 2.3, which combines the AE representation with a standard inexact truncated Gauss-Newton method [19, 27]. Hence the search direction is computed by a truncated CG iteration with the Eisenstat-Walker stopping criterion [13, 24, 26, 10] with $\eta_0 = 0.7$ and standard Armijo step-size control. We recall that no extra Tikhonov-type regularization is added to the objective functional. During frequency continuation, we progressively increase the frequency, ω, always starting at the lowest frequency $\omega = 8$. The number of AE eigenfunctions, K, starts at $K = 32$ and increases linearly as $K = 4\omega$. In the definition of $\mu[u](x)$ in (6), we always set $\varepsilon = 10^{-6}$ and keep all other parameters values fixed to underpin the robustness of the AEI Algorithm.

4.1   Single parameter inversion: piecewise constant medium

Here we consider a single parameter inverse problem with $v \equiv 1$ fixed and shall attempt to recover from boundary data the piecewise constant profile u shown in Fig. 1. Inside
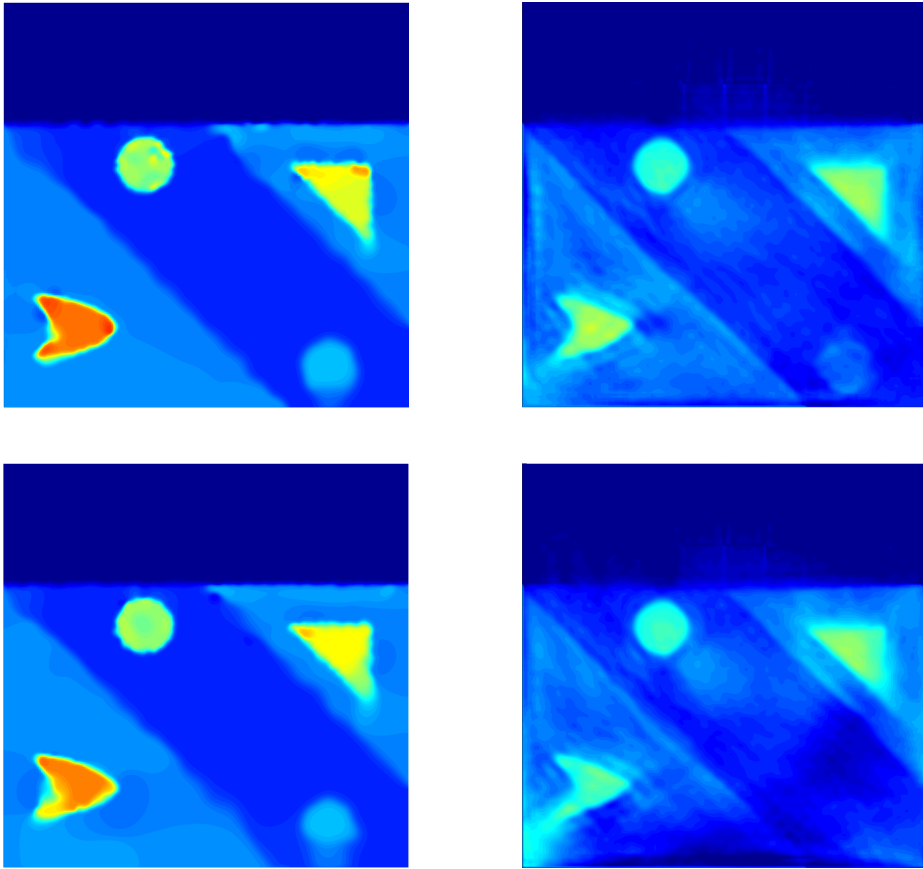
Figure 4: Reconstruction of u: top, full boundary data. Bottom, partial boundary data. The AE approach (left) and the nodal basis approach (right).

Ω, we discretize (2), (5)–(7) on a 300×300 Cartesian mesh and place nine equispaced Gaussian sources along the upper boundary at $(0.1, 0.8), \ldots, (0.9, 0.8)$. With the initial guess simply set to $u(x) \equiv 1$, we start at $\omega = 8$ and progressively increase the frequency as $\omega = 10, 20, 30, \ldots, 120$ together with $K = K_u = 4\omega$. To underline the accuracy of the AE representation, we also compare it to a standard grid-based nodal representation where we add a TV-penalty [39] term with Tikhonov regularization parameter α proportional to the misfit [36].

First, we include boundary data from all four boundaries. The corresponding two reconstructed profiles are shown at the top of Fig. 4. Although both methods recover the essential features of the medium, the AEI approach clearly yields not only sharper boundaries but also more accurate values inside the different subregions, off by at most 10% from the true values. Moreover, the AEI Algorithm achieves the higher accuracy with only $K = 480$ degrees of freedom versus about 180000 for the staggered grid nodal representation.

Next, we repeat the same numerical experiment but omit all the receivers located at the lower boundary of Ω. Hence much less information about the lower part of the medium

13

is available in the data. Unlike the nodal approach, however, the AEI method is still able to recover $u(x)$ throughout Ω, as shown in the lower two frames of Fig. 4. In particular, we observe how the small disk in the lower right corner is no longer visible with the nodal approach. Despite the much smaller number of control variables used in the AEI Algorithm, the reconstruction appears more accurate and more tolerant to missing data.
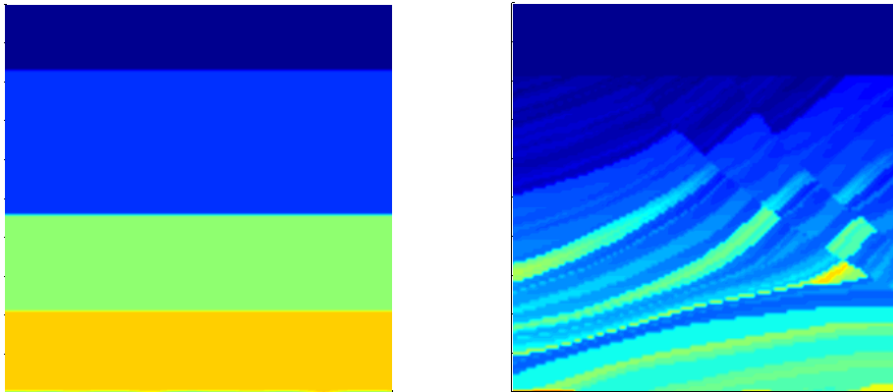

Figure 5: Marmousi profile: the initial guess (left) and the true profile (right).

4.2   Single parameter inversion: Marmousi profile

Next, we consider again a single parameter inverse problem with $v \equiv 1$ fixed and shall attempt to recover from boundary data the well-known Marmousi profile $u(x)$ [21] shown in Fig. 5; it models a typical layered geophysical medium with regions of different wave speed [21]. Due to the complexity of the medium, we now increase the amount of available data by incorporating observations from 201 Gaussian sources located at $(0.1, 0.9), (0.1045, 0.9),$ $(0.109, 0.9) \ldots, (0.9, 0.9)$ near the top boundary. Still, to avoid increasing the computational cost while taking into account all the available data, we use the sample average aproximation (SAA) approach from [20] and replace the 201 sources by six random averages or "super-shots". The receivers are located on the north, east and west boundaries of Ω where we again use a 300×300 equispaced finite-difference mesh. For the initial guess we choose the four-layered profile shown in Fig. 5 and progressively increase $\omega = 8, 12, 16, \ldots, 200$ during frequency continuation.

In Fig. 6, we display four reconstructions each obtained with the AEI Algorithm but using a different AE basis determined by the choice of μ either as in (6), (12), (15) or (18). Despite the poor initial guess, the AEI Algorithm is always able to recover the essential features of the Marmousi profile. Nevertheless, the reconstructions are overly smooth, indicating the need for an AE basis better adapted to the anisotropic layered nature of the medium.

Subsurface models of the Earth are typically layered with rapid variations in the vertical and smooth variations in the horizontal direction. To build an improved AE basis adapted to layered media from seismic imaging, this prior information ought to be incorporated
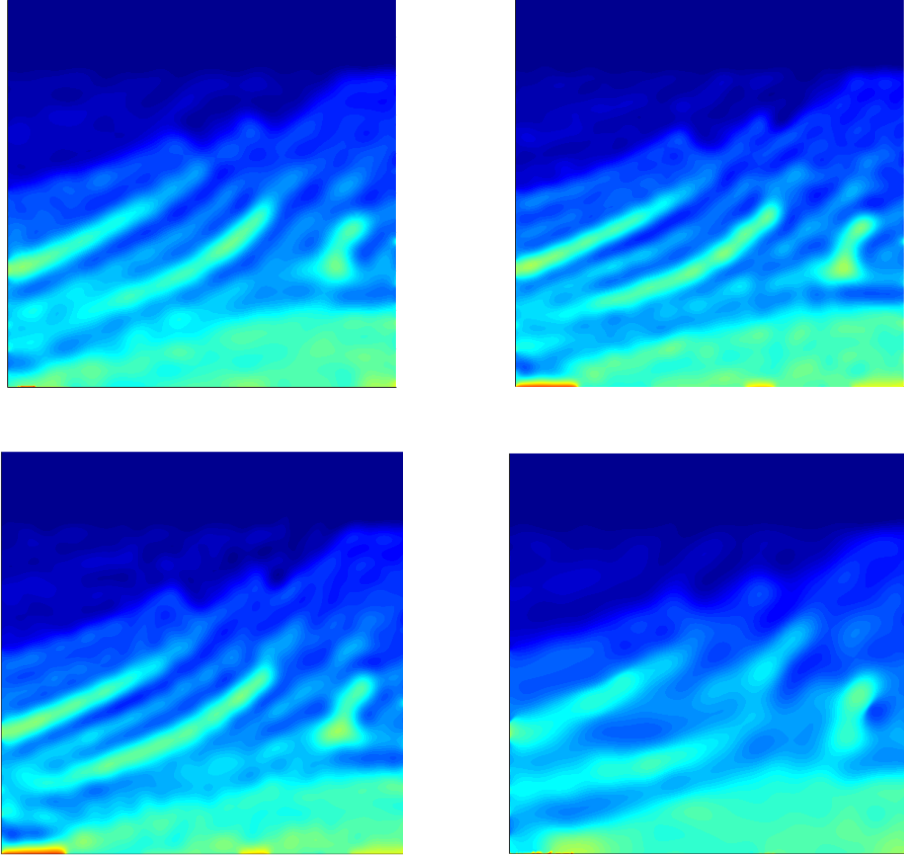
14

Figure 6: Marmousi profile: reconstructions using four different AE bases: TV-regularization, L^2 error = 6.42% (top left), H^1-regularization, L^2 error = 6.43% (top right), Gaussian-regularization, L^2 error = 7.12% (bottom left), Lorentzian-regularization L^2 error = 8.83% (bottom right).

into the optimization process. To do so, we shall now construct the AE basis from TV-regularization applied only to variations in the vertical direction, x_2, by replacing $\mu[u](x)$ in (6) by

$$\mu[u](x_1, x_2) = \left[\left| \frac{\partial u(x_1, x_2)}{\partial x_2} \right|^2 + \varepsilon^2 \right]^{-1/2}. \tag{20}$$

Thus we obtain the corresponding eigenvalue problem:

$$\begin{cases} -\nabla \cdot \left(\dfrac{1}{\sqrt{\left| \frac{\partial u(x)}{\partial x_2} \right|^2 + \varepsilon^2}} \nabla \phi_m(x) \right) = \lambda_m \phi_m(x), & (x_1, x_2) = x \in \Omega, \\ \phi_m(x) = 0, & x \in \Gamma. \end{cases} \tag{21}$$

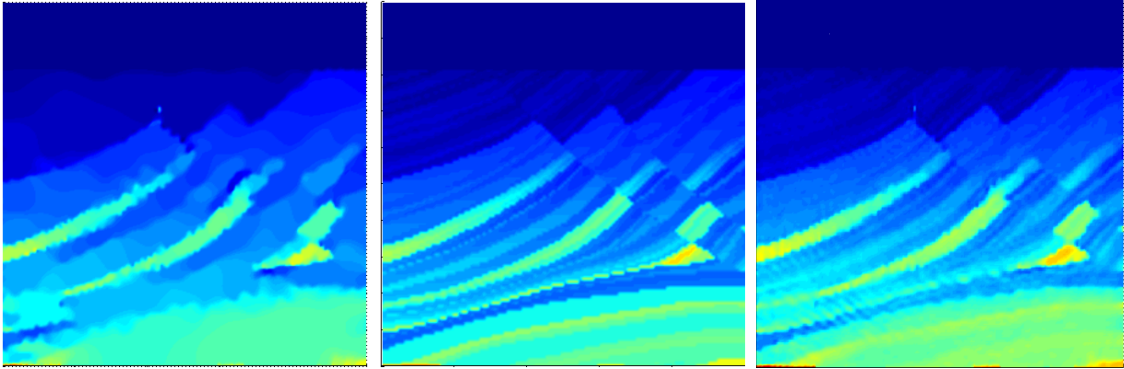The resulting eigenfunctions in (21) take into account the anisotropic TV-penalization in

15

Figure 7: Marmousi profile: the reconstruction using the anisotropic AE basis from (21) and the initial guess in Fig. 5 (left), the true profile (center), the reconstruction using a standard grid-based nodal basis and the initial guess from the anisotropic AE reconstruction shown on the left (right).

the vertical direction. Moreover, in any subregion of Ω where $\partial u/\partial x_2$ vanishes, $\mu = 1/\varepsilon$ is constant, and the eigenvalue problem (21) simplifies to

$$-\Delta\phi_m(x) = (\varepsilon\lambda_m)\phi_m(x)\,.$$

Hence the eigenfunctions locally corresponds to those of the Laplacian, as in (12) for the H^1-penalty functional.

Starting from the same initial guess shown in Fig. 5, we now repeat the above numerical experiment but use the anisotropic AE basis from (21) instead. As shown in the left frame of Fig. 7, the solution respects the material discontinuities in the vertical directions quite accurately, unlike the AEI solutions shown in Fig. (6) while appearing smooth in the horizontal direction.

For even higher fidelity in the reconstruction of complex and detailed media, such as the Marmousi profile, we now resort to a standard grid-based nodal representation of u. For the latter, a sufficiently close initial guess, typically a smooth representation of the target, is needed to ensure convergence [37, 3]. Hence, we now use a standard nodal basis (with over a hundred times more degrees of freedom) for the optimization but use as initial guess the (intermediate) AEI reconstruction in the left frame of Fig. 7. The resulting combined AEI-nodal approach recovers even the finest details, as shown in the right frame of Fig. 7, despite the original poor initial guess from Fig. 5.

4.3   Two-parameter inversion: piecewise constant medium

Finally, we consider the reconstruction of the piecewise constant medium characterized by the two parameters, $u(x)$ and $v(x)$, shown in Fig. 8. Due to the strong coupling between u and v through the scalar forward problem (2), changes in either parameter tend to influence the other, thus leading to undesired "cross-talk" artifacts [28, 23]. We now illustrate the
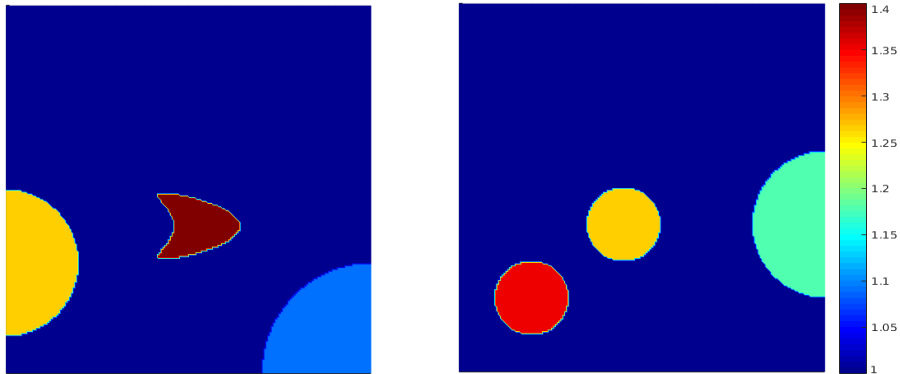
16

Figure 8: Two-parameter piecewise constant medium: u (left) and v (right).

usefulness of the AEI approach in significantly reducing cross-talk by building a distinct basis of eigenfunctions (4) for each parameter.

Again we use observations from 201 equispaced Gaussian sources located along the upper boundary at $(0.1, 0.8)$, ..., $(0.9, 0.8)$ but avoid increasing the computational cost by combining the data into six "super-shots" using the SAA approach [20]. Inside Ω, we discretize (2), (5)-(7) on a 200×200 finite-difference mesh. Both initial profiles are set to a uniform background $u \equiv 1$ and $v \equiv 1$. Starting from $\omega = 8$ we again progressively increase the frequency $\omega = 10, 20, 30, \ldots, 90$ together with the dimensions of the AE subspaces $K_u = K_v = 2\omega$.

In Fig. 9, we compare the reconstructions obtained with the AEI approach versus a standard grid-based nodal representation without added Tikhonov regularization, for simplicity. Although both methods recover the locations of the essential features in the medium, the AEI approach clearly achieves higher accuracy with minimal cross-talk between the two parameters. In particular, we observe that the nodal approach fails to determine the true values of u inside the various obstacles. It also leads to stronger cross-talk artifacts clearly apparent inside the two smaller disk-shaped obstacles in v. In contrast, the reconstructions obtained with the AEI approach display sharper boundaries, little cross-talk and rather accurate values of u and v throughout Ω.

Next, we repeat the previous numerical experiment but now set the initial values for u and v to

$$\begin{cases} u(x) = 1.4 & x \in B\,, \\ u(x) = 1 & x \in \Omega \backslash B\,, \end{cases} \qquad \begin{cases} v(x) = 1 & x \in \Omega\,, \end{cases}$$

where B denotes the disk of radius 0.2 centered at $(0.55, 0.4)$. The initial values for u and v, shown at the top of Fig. 10, are intended to facilitate the recovery of the kite-shaped obstacle inside u, in particular, whose value and location coincide with those inside the disk B.

As shown in Fig. 10, the new initial value for u helps both the nodal and the AEI based approach in recovering the kite-shaped obstacle more accurately. However, the new starting value for u greatly perturbs the overall reconstruction using the nodal approach,
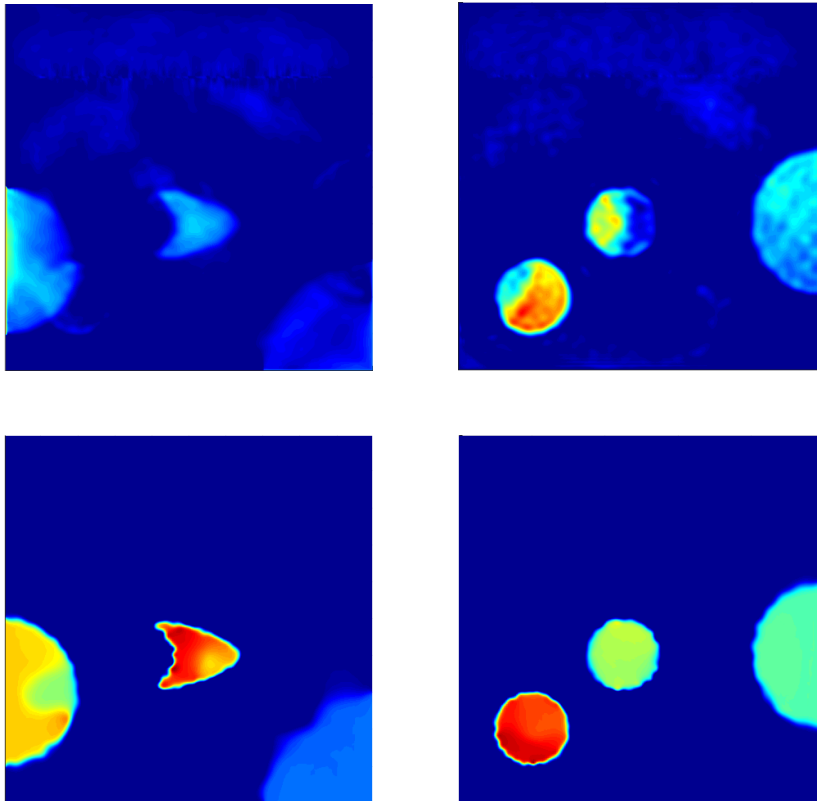
17

Figure 9: Two-parameter piecewise constant medium u (left) and v (right): reconstructions using a grid-based nodal approach (top) or the AEI approach (bottom).

as the initial condition not only remains clearly visible inside u but also appears inside v, where it remains throughout the optimization process. Moreover, the quarter circle in u located in the lower right corner of Ω is now barely visible while further cross-talk due to the kite in u appears also inside v. Hence, a simple change in initial conditions strongly influences the outcome of the optimizationusing the grid-based nodal approach which is, at the least, unsatisfactory.

In contrast, the modified initial conditions have little effect on the reconstructions in Figs. 9 and 10 using the AEI approach: the initial disk B no longer appears inside the final reconstructions, shown at the bottom of Fig. 10, with slight perturbations near the kite, though the value of the centered smaller disk-shaped obstacle inside v is somewhat higher than in the true profile. In that sense, the AEI approach clearly appears more robust not only to missing data – see Section 4.1 – but also to the particular choice of initial condition. Moreover, it reduces the amount of cross-talk, if any, quite significantly.
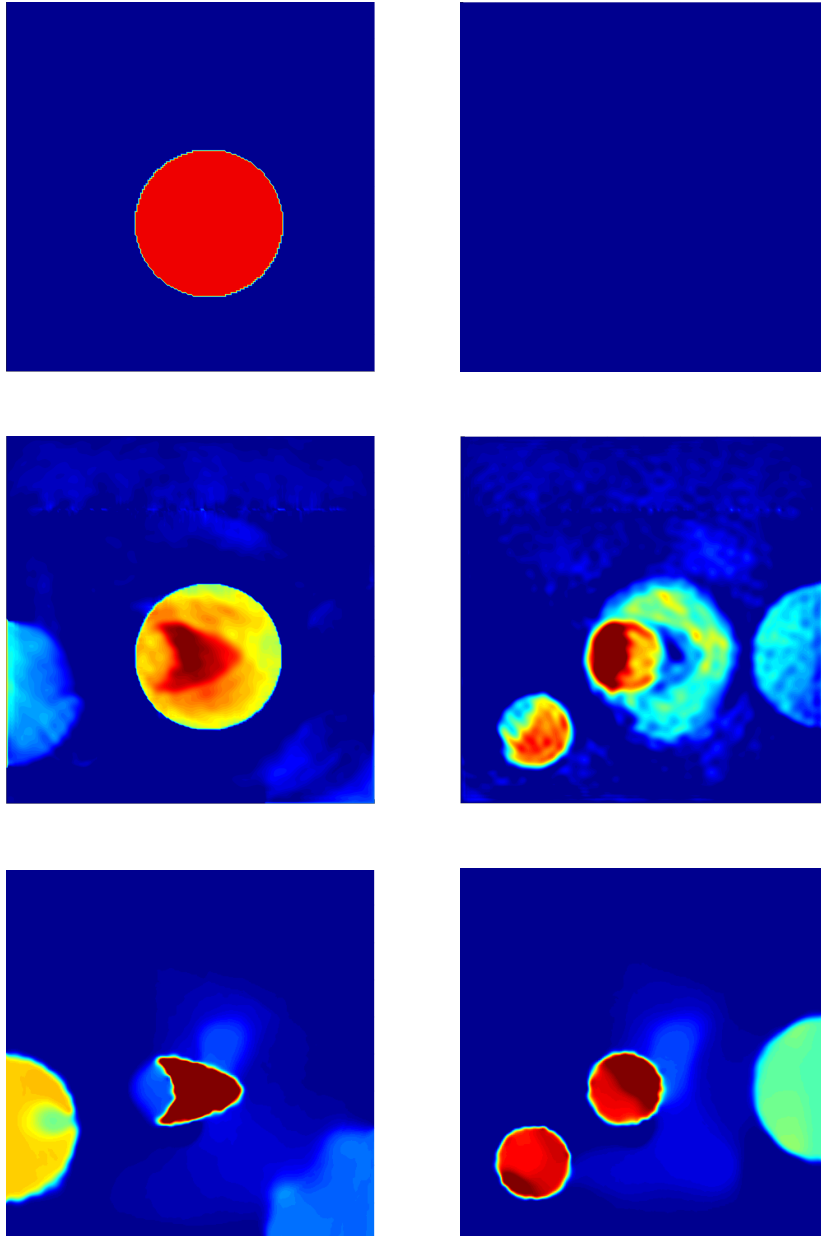
18

Figure 10: Two-parameter piecewise constant medium u (left) and v (right): initial guess (top); reconstructions using a grid-based nodal basis (middle) or an AE basis (bottom).
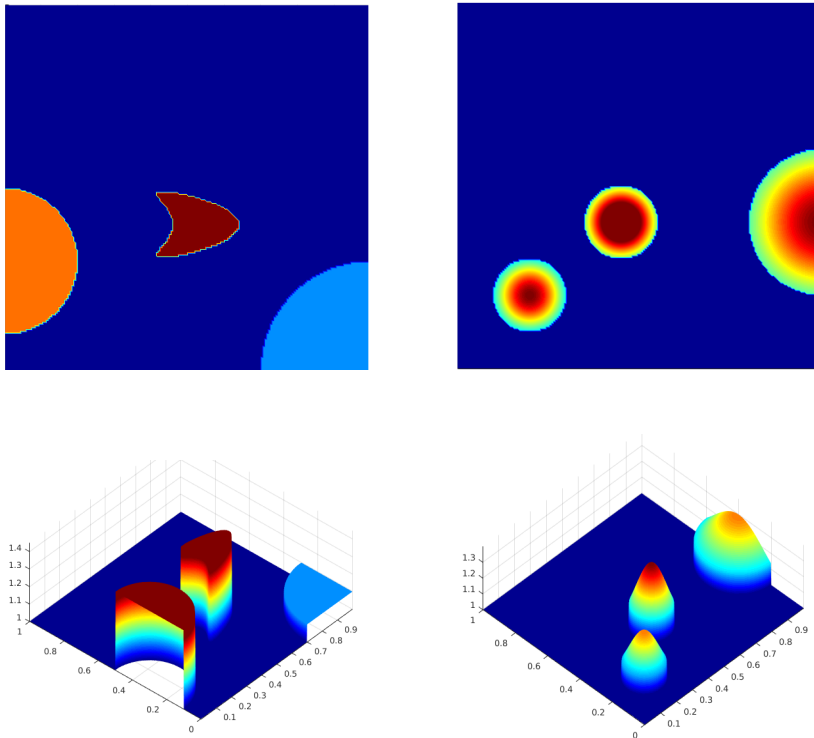
Figure 11: Two-parameter medium u (left) and v (right) with distinct regularity properties: Two-dimensional view (top) and three-dimensional view (bottom).

4.4   Two-parameter inversion: distinct regularity properties

Finally, we consider a medium inside Ω again characterized by two parameters $u(x)$ and $v(x)$, yet with distinct regularity properties: while u again corresponds to the previous piecewise constant profile, the variations in v are now smooth, as shown in Fig. 11.

The distinct regularity properties of u and v, assumed to be known a priori, demand distinct types of regularization for each parameter. To incorporate this prior information into the optimization, we thus choose separate AE bases to represent u and v, each derived from a distinct penalty functional. Hence, we expand u and v as in (4), where ϕ_m are the eigenfunctions corresponding to the TV-penalization functional (7) with μ as in (6) and $\varepsilon = 10^{-6}$, whereas φ_l are the (Laplacian) eigenfunctions corresponding to the H^1-penalization functional in (12). Similarly, for the nodal basis approach, we add here a Tikhonov-type TV-penalty term for u and an H^1-penalty term for v (3). All other parameter settings for the numerical experiments remain identical to those in Section 4.3 except that we now use a finer 500×500 mesh.

In Fig. 12, we display the reconstructions for the standard grid-based nodal representation and for the AEI approach. Again, both methods recover the essential features present in the medium. The grid-based nodal approach, however, fails to determine the true values of u or v inside the various obstacles while the outline of the leftmost half disk in u appears also in v cutting off the smaller disk in the lower left corner. In contrast, the AEI approach
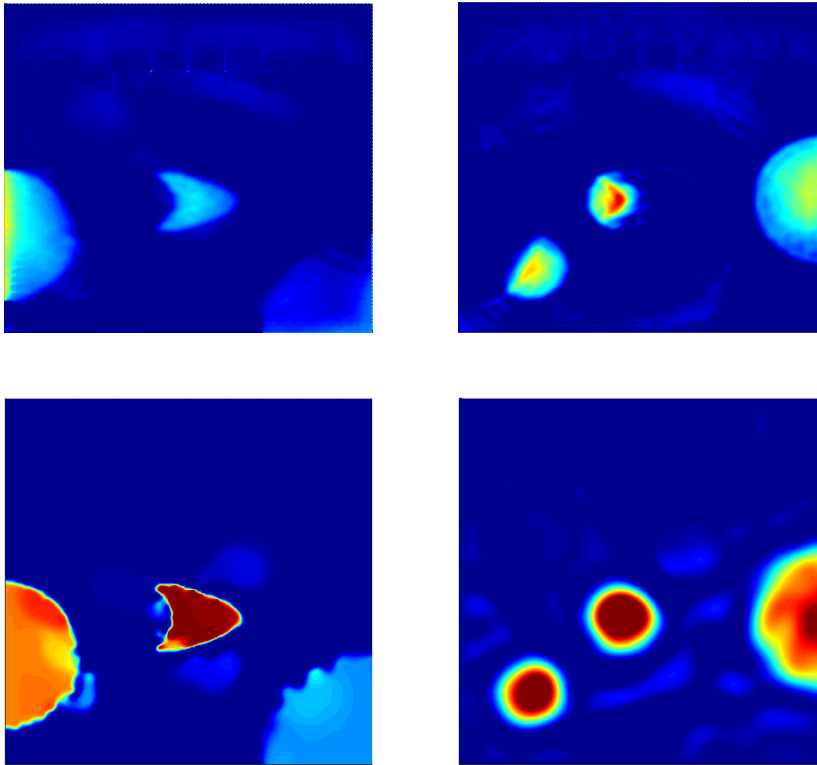
20

Figure 12: Two-parameter profile u (left) and v (right) with distinct regularity properties: reconstructions using a grid-based nodal representation (top) or two distinct AE bases (bottom).

clearly achieves much higher accuracy with little cross-talk between the two parameters. Moreover, the boundaries of the various obstacles in u are clearly sharper than those in v, where even the smooth variations inside the rightmost half-circle are visible. Hence selecting separate eigenspaces for individual parameters, possibly derived from distinct penalty functionals, not only increases robustness by efficiently regularizing the inversion, but also significantly reduces the presence of cross-talk between the various parameters.

5 Concluding remarks

We have presented a nonlinear optimization method for the solution of inverse scattering problems in the frequency domain, when the unknown medium is characterized by one or several parameters $u(x), v(x), \ldots$ The time-harmonic inverse medium problem is formulated as a PDE-constrained optimization problem and solved by an inexact truncated Newton or quasi-Newton iteration. Instead of a standard (FD or FE) grid-based nodal representation, each unknown spatially varying parameter is represented as a linear combination of a "background" u_0 which solves (5) and the first K_u (orthogonal) eigenfunctions ϕ_m of the elliptic eigenvalue problem (7). During the optimization process, which may

include frequency continuation, the bases $u_0 \cup \{\phi_1, \ldots, \phi_{K_u}\}$, $v_0 \cup \{\varphi_1, \ldots, \varphi_{K_v}\}, \ldots$ and their respective dimensions are repeatedly adapted to the current iterates. The full Adaptive Eigenspace Inversion (AEI) Algorithm for two spatially varying parameters $u(x), v(x)$ is given in Section 2.3; its generalization to three or more parameters is immediate.

The AEI Algorithm inherently builds regularization into the optimization by restricting the search for each parameter $u(x)$ to an individual subspace, V_K, spanned by $u_0 \cup \{\phi_1, \ldots, \phi_K\}$. As the governing wave length decreases during frequency continuation, we increase the dimension of V_K to accomodate the more detailed small-scale information about the scatterer which is progressively revealed. The elliptic differential operator that appears in the eigenvalue problem (7) with $\mu[u]$ as in (6) corresponds to the gradient of the standard total variation penalty functional (9). By exhibiting the fundamental connection between Tikhonov regularization and the AE basis, we have not only underpinned the remarkable accuracy of the AE representation, but also opened up new possibilities in devising AE bases. Thus whenever a priori information about the scatterer hints at a judicious penalty functional $\mathcal{R}(u)$ for Tikhonov regularization, the corresponding AE eigenfunction representation determined by $\nabla_u \mathcal{R}(u)$ may be used instead for a more efficient and robust inversion.

Although the AEI method uses much fewer control variables for each parameter, the reconstructions are remarkably accurate, usually more so than grid-based nodal representations, display less artifacts and prove more tolerant to missing data. For multi-parameter inverse problems, in particular, the AEI approach significantly reduces spurious "crosstalk" between different parameters. The AEI Algorithm has also proved remarkably robust with respect to the choice of parameters or initial conditions. Since the discrete version of the eigenvalue problem (7) leads to a sparse, symmetric and positive definite matrix, the first K eigenfunctions can be efficiently computed via a standard Lanczos iteration. If finite element mesh adaptation is used for the numerical solution of (7), small-scale features and interfaces are captured with even greater accuracy in the reconstruction, without increasing the computational effort. Although the eigenfunctions are global, their information content is highly localized in space so that most entries can in fact be neglected, as shown in [18].

The AE basis depends only on the regularization and not on the underlying forward problem considered. Therefore, it is likely that the AE representation will also prove useful for single and multi-parameter inverse problems governed by other elliptic or time dependent partial differential equations.

Acknowledgment

References

[1] A. Asnaashari, R. Brossier, S. Garambois, F. Audebert, P. Thore, and J. Virieux. Regularized seismic full waveform inversion with prior model information. *Geophysics*, 78(2):R25–R36, 2013.

[2] G. Bao and J. Lin. Imaging of local surface displacement on an infinite ground plane: The multiple frequency case. *SIAM Journal on Applied Mathematics*, 71(5):1733–1752, 2011.

[3] R. Brossier, S. Operto, and J. Virieux. Seismic imaging of complex onshore structures by 2D elastic frequency-domain full-waveform inversion. *Geophysics*, 74(6):WCC105–WCC118, 2009.

[4] F. Cakoni and D. L. Colton. *Qualitative methods in inverse scattering theory: an introduction*. Interaction of mechanics and mathematics series. Springer, 2006.

[5] G. Chavent. *Nonlinear Least Squares for Inverse Problems*. Springer Science & Business Media, 1996.

[6] Y. Chen. Inverse scattering via Heisenberg's uncertainty principle. *Inverse Problems*, 13(2):253, 1997.

[7] M. de Buhan and M. Darbas. Numerical resolution of an electromagnetic inverse medium problem at fixed frequency. *Computers and Mathematics with Applications*, in press.

[8] M. de Buhan and M. Kray. A new approach to solve the inverse scattering problem for waves: combining the TRAC and the Adaptive Inversion methods. *Inverse Problems*, 29(8):085009, 2013.

[9] M. de Buhan and A. Osses. Logarithmic stability in determination of a 3D viscoelastic coefficient and a numerical example. *Inverse Problems*, 26(9):95006, 2010.

[10] R. S. Dembo and T. Steihaug. Truncated-Newton algorithms for large-scale unconstrained optimization. *Mathematical Programming*, 26(2):190–212, 1983.

[11] D. C. Dobson and F. Santosa. Recovery of blocky images from noisy and blurred data. *SIAM Journal on Applied Mathematics*, 56(4):1181–1198, 1996.

[12] S. Durand and M. Nikolova. Stability of the minimizers of least squares with a nonconvex regularization. part i: Local behavior. *Applied Mathematics and Optimization*, 53(2):185–208, 2006.

[13] S. C. Eisenstat and H. F. Walker. Choosing the forcing terms in an inexact Newton method. *SIAM J. Sci. Comput.*, 17(1):16–32, 1996.

23

[14] H. W. Engl, M. Hanke, and A. Neubauer. *Regularization of inverse problems*, volume 375. Springer Science & Business Media, 1996.

[15] A. L. Gallardo and M. A. Max. Joint two-dimensional DC resistivity and seismic travel time inversion with cross-gradients constraints. *Journal of Geophysical Research*, 109(B3), 2004.

[16] G. H. Golub, P. C. Hansen, and D. P. O'Leary. Tikhonov regularization and total least squares. *SIAM Journal on Matrix Analysis and Applications*, 21(1):185–194, 1999.

[17] M. J. Grote, J. Huber, D. Kourounis, and O. Schenk. Inexact interior-point method for PDE-constrained nonlinear optimization. *SIAM J. Sci. Comp.*, 36(3):A1251–A1276, 2014.

[18] M. J. Grote, M. Kray, and U. Nahum. Adaptive eigenspace method for inverse scattering problems in the frequency domain. *Inv. Problems*, 33:025006, 2017.

[19] E. Haber, U. M. Ascher, and D. Oldenburg. On optimization techniques for solving nonlinear inverse problems. *Inverse Problems*, 16:1263, 2000.

[20] E. Haber and M. Chung. Simultaneous source for non-uniform data variance and missing data. available on arXiv:1404.5254, submitted in 2014.

[21] T. Irons. Marmousi model. 1988. www.reproducibility.org/RSF/book/data/marmousi/paper.pdf.

[22] R. B. Lehoucq and D. C. Sorensen. Deflation techniques for an implicitly re-started Arnoldi iteration. *SIAM J. Matrix Anal. Appl*, 17:789–821, 1996.

[23] L. Métivier, F. Bretaudeau, R. Brossier, S. Operto, and J. Virieux. Full waveform inversion and the truncated Newton method: quantitative imaging of complex subsurface structures. *Geophysical Prospecting*, 62(6):1353–1375, 2014.

[24] L. Métivier, R. Brossier, J. Virieux, and S. Operto. Full waveform inversion and the truncated Newton method. *SIAM J. Sci. Comput.*, 35(2):B401–B437, 2013.

[25] U. Nahum. *Adaptive eigenspace for inverse problems in the frequency domain.* PhD thesis, University of Basel, 2016.

[26] S. G. Nash. A survey of truncated-Newton methods. *J. Comput. Appl. Math.*, 124(1-2):45–59, 2000.

[27] J. Nocedal and S. J. Wright. *Numerical Optimization.* Springer, New York, 2 edition, 2006.

[28] W. Pan and K. Innanen. Suppress parameter cross-talk for elastic full-waveform inversion: Parametrization and acquisition geometry. *GeoConvention*, 2016.

[29] B. Peters and F. J. Hermann. A sparse reduced Hessian approximation for multi-parameter wavefield reconstruction inversion. *SEG Denver Annual Meeting*, 2014.

[30] R. G. Pratt. Seismic waveform inversion in the frequency domain, part 1: Theory and verification in a physical scale model. *Geophysics*, 64(3):888–901, 1999.

[31] R. G. Pratt, C. Shin, and G. J. Hicks. Gauss-Newton and full Newton methods in frequency-space seismic waveform inversion. *Geophys. J. Int.*, 133(2):341–362, 1998.

[32] V. Prieux, R. Brossier, S. Operto, and J. Virieux. Multiparameter full waveform inversion of multicomponent Ocean-Bottom-Cable data from Valhall field. Part 1: imaging compressional wave speed, density and attenuation. *Geophys. J. Int.*, 194(3):1640–1664, 2013.

[33] L. I. Rudin, S. Osher, and E. Fatemi. Nonlinear total variation based noise removal algorithms. *Physica D: Nonlinear Phenomena*, 60(1):259–268, 1992.

[34] A. Tarantola. Inversion of seismic reflection data in the acoustic approximation. *Geophysics*, 49(8):1259–1266, 1984.

[35] A. N. Tikhonov. On the stability of inverse problems. *Dokl. Akad. Nauk SSSR*, 39(5):195–198, 1943.

[36] P. M. van den Berg, A. Abubakar, and J. T. Fokkema. Multiplicative regularization for contrast profile inversion. *Radio Science*, 38(2):n/a–n/a, 2003. 8022.

[37] J. Virieux and S. Operto. An overview of full-waveform inversion in exploration geophysics. *Geophysics*, 74(6):WCC1–WCC26, 2009.

[38] C. Vogel. *Computational Methods for Inverse Problems*. Society for Industrial and Applied Mathematics, 2002.

[39] C. R. Vogel and E. Oman. Iterative methods for total variation denoising. *SIAM J. Sci. Comput.*, 17(1):227–238, 1996.

LATEST PREPRINTS

No.	Author: *Title*

2016-21   **A. Hyder, S. Iula, L. Martinazzi**
Large blow-up sets for the prescribed Q-curvature equation in the Euclidean space

2016-22   **P. Habegger**
The norm of Gaussian periods

2016-23   **P. Habegger**
Diophantine approximations on definable sets

2016-24   **F. Amoroso, D. Masser**
Lower bounds for the height in Galois extensions

2016-25   **W. D. Brownawell, D. W. Masser**
Zero estimates with moving targets

2016-26   **H. Derksen, D. Masser**
Linear equations over multiplicative groups, recurrences, and mixing III

2016-27   **D. Bertrand, D. Masser, A. Pillay, U. Zannier**
Relative Manin-Mumford for semi-abelian surfaces

2016-28   **L. Capuano, D. Masser, J. Pila, U. Zannier**
Rational points on Grassmannians and unlikely intersections in tori

2016-29   **C. Nobili, F. Otto**
Limitations of the background field method applied to Rayleigh-Bénard convection

2016-30   **W. D. Brownawell, D. W. Masser**
Unlikely intersections for curves in additive groups over positive characteristic

2016-31   **M. Dambrine, H. Harbrecht, M. D. Peters, B. Puig**
On Bernoulli's free boundary problem with a random boundary

2016-32   **H. Harbrecht, J. Tausch**
A fast sparse grid based space-time boundary element method for the nonstationary heat equation

2016-33   **S. Iula**
A note on the Moser-Trudinger inequality in Sobolev-Slobodeckij spaces in dimension one

---

Preprints are available under *https://math.unibas.ch/research/publications*

LATEST PREPRINTS

No.	**Author:** *Title*

2016-34   **C. Bürli, H. Harbrecht, P. Odermatt, S. Sayasone, N. Chitnis**
Mathematical analysis of the transmission dynamics of the liver fluke, Opisthorchis viverrini

2017-01   **J. Dölz and T. Gerig, M. Lüthi, H. Harbrecht and T. Vetter**
Efficient computation of low-rank Gaussian process models for surface and image registration

2017-02   **M. J. Grote, M. Mehlin, S. A. Sauter**
Convergence analysis of energy conserving explicit local time-stepping methods for the wave equation

2017-03   **Y. Bilu, F. Luca, D. Masser**
Collinear CM-points

2017-04   **P. Zaspel**
Ensemble Kalman filters for reliability estimation in perfusion inference

2017-05   **J. Dölz and H. Harbrecht**
Hierarchical Matrix Approximation for the Uncertainty Quantification of Potentials on Random Domains

2017-06   **P. Zaspel**
Analysis and parallelization strategies for Ruge-Stüben AMG on many-core processors

2017-07   **H. Harbrecht and M. Schmidlin**
Multilevel Methods for Uncertainty Quantification of Elliptic PDEs with Random Anisotropic Diffusion

2017-08   **M. Griebel and H. Harbrecht**
Singular value decomposition versus sparse grids: Refined complexity Estimates

2017-09   **J. Garcke and I. Kalmykov**
Efficient Higher Order Time Discretization Schemes for Hamilton-Jacobi-Bellman Equations Based on Diagonally Implicit Symplectic Runge-Kutta Methods

2017-10   **M. J. Grote and U. Nahum**
Adaptive Eigenspace Regularization For Inverse Scattering Problems

---

Preprints are available under *https://math.unibas.ch/research/publications*